

SEARCH FOR VERY HIGH ENERGY GAMMA RAYS FROM THE NORTHERN *FERMI* BUBBLE REGION WITH HAWC

A.U. ABEYSEKARA,¹ A. ALBERT,² R. ALFARO,³ C. ALVAREZ,⁴ J.D. ÁLVAREZ,⁵ R. ARCEO,⁴ J.C. ARTEAGA-VELÁZQUEZ,⁵ H.A. AYALA SOLARES,⁶ A.S. BARBER,⁷ N. BAUTISTA-ELIVAR,⁸ A. BECERRIL,³ E. BELMONT-MORENO,³ S.Y. BENZVI,⁹ D. BERLEY,¹⁰ J. BRAUN,¹¹ C. BRISBOIS,⁶ K.S. CABALLERO-MORA,⁴ T. CAPISTRÁN,¹² A. CARRAMIÑANA,¹² S. CASANOVA,¹³ M. CASTILLO,⁵ U. COTTI,⁵ J. COTZOMI,¹⁴ S. COUTIÑO DE LEÓN,¹² C. DE LEÓN,¹⁴ E. DE LA FUENTE,¹⁵ R. DIAZ HERNANDEZ,¹² B.L. DINGUS,² M.A. DUVERNOIS,¹¹ J.C. DÍAZ-VÉLEZ,¹⁵ R.W. ELLSWORTH,¹⁶ K. ENGEL,¹⁰ B. FICK,¹⁷ D.W. FIORINO,¹⁰ N. FRAIJA,¹⁸ J.A. GARCÍA-GONZÁLEZ,³ F. GARFIAS,¹⁸ M. GERHARDT,⁶ A. GONZÁLEZ MUÑOZ,³ M.M. GONZÁLEZ,¹⁸ J.A. GOODMAN,¹⁰ Z. HAMPEL-ARIAS,¹¹ J.P. HARDING,² S. HERNANDEZ,³ A. HERNANDEZ-ALMADA,³ J. HINTON,¹⁹ B. HONA,⁶ C.M. HUI,²⁰ P. HÜNTEMAYER,⁶ A. IRIARTE,¹⁸ A. JARDIN-BLICQ,¹⁹ V. JOSHI,¹⁹ S. KAUFMANN,⁴ A. LARA,²¹ R.J. LAUER,²² W.H. LEE,¹⁸ D. LENNARZ,²³ H. LEÓN VARGAS,³ J.T. LINNEMANN,²⁴ A.L. LONGINOTTI,¹² G. LUIS RAYA,⁸ R. LUNA-GARCÍA,²⁵ R. LÓPEZ-COTO,¹⁹ K. MALONE,²⁶ S.S. MARINELLI,²⁴ O. MARTINEZ,¹⁴ I. MARTINEZ-CASTELLANOS,¹⁰ J. MARTÍNEZ-CASTRO,²⁵ H. MARTÍNEZ-HUERTA,²⁷ J.A. MATTHEWS,²² P. MIRANDA-ROMAGNOLI,²⁸ E. MORENO,²⁹ M. MOSTAFÁ,²⁶ L. NELLEN,³⁰ M. NEWBOLD,⁷ M.U. NISA,⁹ R. NORIEGA-PAPAQUI,²⁸ R. PELAYO,²⁵ J. PRETZ,²⁶ E.G. PÉREZ-PÉREZ,⁸ Z. REN,²² C.D. RHO,⁹ C. RIVIÈRE,¹⁰ D. ROSA-GONZÁLEZ,¹² M. ROSENBERG,²⁶ E. RUIZ-VELASCO,³ H. SALAZAR,¹⁴ F. SALESA GREUS,¹³ A. SANDOVAL,³ M. SCHNEIDER,³¹ H. SCHOORLEMMER,¹⁹ G. SINNIS,² A.J. SMITH,¹⁰ R.W. SPRINGER,⁷ P. SURAJBALI,¹⁹ I. TABOADA,²³ O. TIBOLLA,⁴ K. TOLLEFSON,²⁴ I. TORRES,¹² T.N. UKWATTA,² G. VIANELLO,³² T. WEISGARBER,¹¹ S. WESTERHOFF,¹¹ I.G. WISHER,¹¹ T. YAPICI,²⁴ G.B. YODH,³³ A. ZEPEDA,^{4,27} AND H. ZHOU²

¹Department of Physics and Astronomy, University of Utah, Salt Lake City, UT, USA

²Physics Division, Los Alamos National Laboratory, Los Alamos, NM, USA

³Instituto de Física, Universidad Nacional Autónoma de México, Mexico City, Mexico

⁴Universidad Autónoma de Chiapas, Tuxtla Gutiérrez, Chiapas, Mexico

⁵Universidad Michoacana de San Nicolás de Hidalgo, Morelia, Mexico

⁶Department of Physics, Michigan Technological University, Houghton, MI, USA

⁷Department of Physics and Astronomy, University of Utah, Salt Lake City, UT, USA

⁸Universidad Politécnica de Pachuca, Pachuca, Hidalgo, Mexico

⁹Department of Physics & Astronomy, University of Rochester, Rochester, NY, USA

¹⁰Department of Physics, University of Maryland, College Park, MD, USA

¹¹Department of Physics, University of Wisconsin-Madison, Madison, WI, USA

¹²Instituto Nacional de Astrofísica, Óptica y Electrónica, Tonantzintla, Puebla, Mexico

¹³Instytut Fizyki Jadrowej im Henryka Niewodniczańskiego Polskiej Akademii Nauk, Krakow, Poland

¹⁴Facultad de Ciencias Físico Matemáticas, Benemérita Universidad Autónoma de Puebla, Puebla, Mexico

¹⁵Departamento de Física, Centro Universitario de Ciencias Exactas e Ingenierías, Universidad de Guadalajara, Guadalajara, Mexico

¹⁶School of Physics, Astronomy, and Computational Sciences, George Mason University, Fairfax, VA, USA

¹⁷Department of Physics, Michigan Technological University, Houghton, MI, USA

¹⁸Instituto de Astronomía, Universidad Nacional Autónoma de México, Mexico City, Mexico

¹⁹Max-Planck Institute for Nuclear Physics, Heidelberg, Germany

²⁰NASA Marshall Space Flight Center, Astrophysics Office, Huntsville, AL, USA

²¹Instituto de Geofísica, Universidad Nacional Autónoma de México, Mexico City, Mexico

²²Department of Physics and Astronomy, University of New Mexico, Albuquerque, NM, USA

²³School of Physics and Center for Relativistic Astrophysics - Georgia Institute of Technology, Atlanta, GA, USA

²⁴Department of Physics and Astronomy, Michigan State University, East Lansing, MI, USA

²⁵Centro de Investigación en Computación, Instituto Politécnico Nacional, Mexico City, Mexico

²⁶Department of Physics, Pennsylvania State University, University Park, PA, USA

²⁷ *Physics Department, Centro de Investigacion y de Estudios Avanzados del IPN, Mexico City, Mexico*

²⁸ *Universidad Autónoma del Estado de Hidalgo, Pachuca, Mexico*

²⁹ *Facultad de Ciencias Físico Matemáticas, Benemérita Universidad Autónoma de Puebla, Puebla, Mexico*

³⁰ *Instituto de Ciencias Nucleares, Universidad Nacional Autónoma de México, Mexico City, Mexico*

³¹ *Santa Cruz Institute for Particle Physics, University of California, Santa Cruz, Santa Cruz, CA, USA*

³² *Department of Physics, Stanford University, Stanford, CA, USA*

³³ *Department of Physics and Astronomy, University of California, Irvine, Irvine, CA, USA*

ABSTRACT

We present a search of very high energy gamma-ray emission from the Northern *Fermi* Bubble region using data collected with the High Altitude Water Cherenkov (HAWC) gamma-ray observatory. The size of the data set is 290 days. No significant excess is observed in the Northern *Fermi* Bubble region, hence upper limits above 1 TeV are calculated. The upper limits are between $3 \times 10^{-7} \text{ GeV cm}^{-2} \text{ s}^{-1} \text{ sr}^{-1}$ and $4 \times 10^{-8} \text{ GeV cm}^{-2} \text{ s}^{-1} \text{ sr}^{-1}$. The upper limits disfavor a proton injection spectrum that extends beyond 100 TeV without being suppressed. They also disfavor a hadronic injection spectrum derived from neutrino measurements.

Keywords: Astroparticle physics — gamma rays — *Fermi* Bubbles — Gamma-Ray Astronomy

1. INTRODUCTION

The search for a counterpart of the microwave haze (Dobler et al. 2010) in gamma-ray data, using the *Fermi* Large Area Telescope (LAT), revealed the existence of two large structures extending up to 55° above and below the Galactic Plane (Dobler et al. 2010; Su et al. 2010). Due to their bubble-like shape they received the name of *Fermi* Bubbles.

The gamma-ray emission of the *Fermi* Bubbles presents a hard spectrum $-dN/dE \sim E^{-2}$ in the energy range from approximately 1 GeV to 100 GeV. The surface brightness is roughly uniform in both bubbles—except for a structure inside the South Bubble called the cocoon—and the total luminosity of the bubbles for galactic longitude $|b| > 10^\circ$ and between 100 MeV and 500 GeV was found to be $4.4_{-0.9}^{+2.4} \times 10^{37}$ erg s $^{-1}$ (Ackermann et al. 2014).

The origin of the *Fermi* Bubbles is still uncertain. Different models have been proposed to explain their formation. Most of the models revolve around the idea of outflows from the galactic center which then interact with the interstellar medium. The outflow can be generated by active galactic nucleus activity of our galaxy producing a jet (Guo & Mathews 2012; Guo et al. 2012), wind from long time-scale star formation (Crocker & Aharonian 2011), periodic star capture processes by the supermassive black hole in the Galactic Center (Cheng et al. 2011), or by winds produced by the hot accretion flow in Sgr A* (Mou et al. 2015).

The production of gamma rays is also under dispute. Hadronic and leptonic models are the main mechanisms to explain the gamma-ray production. Photons of hadronic origin are due to the decay of neutral pions that are produced in the interaction of protons with nuclei in the interstellar medium (ISM). These protons are injected in the bubble regions by the outflow processes mentioned before or they can be accelerated inside the bubble as proposed by Fujita et al. (2013, 2014). Some of these models, (Crocker & Aharonian 2011; Fujita et al. 2013), predict the possibility of high-energy gamma rays. In the leptonic model, high-energy photons are produced by inverse Compton scattering from the interaction of energetic electrons with photons from the interstellar radiation fields (IRF) or cosmic microwave background (CMB). The division between hadronic and leptonic models should not be strict, but rather, a combination of both models can be possible as shown in Cheng et al. (2011); Ackermann et al. (2014). Observations at other wavelengths, specifically at lower energies, have helped to constrain some models. For instance, the microwave haze—produced by synchrotron radiation—can help to constrain the electron population, which

can also radiate in gamma rays (Dobler et al. 2010; Su et al. 2010; Crocker & Aharonian 2011; Mou et al. 2015; Guo et al. 2012).

The same principle can apply at very high energies (VHE; >100 GeV), where observations can constrain the population of the highest-energy cosmic rays. Considering that the Northern *Fermi* Bubble region is in the field of view of the High Altitude Water Cherenkov (HAWC), a search for VHE gamma rays (above 1 TeV) is presented. The paper is divided as follows: The HAWC observatory and the data set used in the analysis are defined in Section 2, the analysis procedure is depicted in Section 3, and the results are discussed in Section 4 and summarized in Section 5.

2. THE HAWC OBSERVATORY & THE DATA SET

HAWC is a ground-based gamma-ray observatory. It is located between Volcán Sierra Negra and Pico de Orizaba near Puebla, Mexico, at an altitude of 4100 m a.s.l. and at ($18^\circ 59' 41''$ N, $97^\circ 18' 30''$ W). The observatory has a duty cycle of $>95\%$ and a large field of view of ~ 2 sr, which allows it to cover 8.4 sr in a day (Abeysekara et al. 2013). The instrument consists of an array of 300 water Cherenkov detectors (WCDs). The WCDs are steel tanks of 7.3 m in diameter and 5 m in height, filled with water up to 4.5 m. Each WCD is filled with $\sim 200,000$ L of purified water. The array provides an effective area of $\sim 22,000$ m 2 . Inside the WCDs, four photomultiplier tubes (PMTs) facing upward are attached to the bottom.

A simple multiplicity trigger is applied to find extensive air showers in the data. For the present analysis, the trigger requires 28 PMTs detecting Cherenkov light within a 150 ns time window to be activated in order to identify a shower event. After the processing and calibration of the events, the air shower cores, footprint brightness in the array, and gamma- and cosmic-ray directions are reconstructed. More information on the detector, calibration, and reconstruction is presented in Abeysekara et al. (2017b).

The HAWC observatory began science operations in August 2013, when it was still under construction. The analysis described in this paper uses data between 2014 November 27th to 2016 February 11th.

The data set is divided into seven event-size bins represented by the fraction f of functioning PMT channels triggered in an air shower event. The energy of the observed gamma rays is related to the shower event size that is measured in the HAWC array. The range of f for this analysis goes from 0.162 to 1.00. Table 1 shows the ranges for each analysis bin.

Table 1. Analysis Bins defined as the fraction of operational PMT channels triggered in an air shower event.

Analysis Bin	f
f_1	0.162 - 0.247
f_2	0.247 - 0.356
f_3	0.356 - 0.485
f_4	0.485 - 0.618
f_5	0.618 - 0.740
f_6	0.740 - 0.840
f_7	0.840 - 1.00

Standard selection cuts are applied to the data that pass the trigger condition. The signals in each PMT should have >1 photoelectrons (PEs) and should be 150 ns before and 400 ns after the trigger. In addition, it is required that more than 90% of the PMT channels are functioning during the observation. Finally, cuts are applied to distinguish between gamma rays and hadronic cosmic rays, the latter being the main background of measurements with the HAWC observatory. All the cuts are optimized by studying the Crab Nebula in the HAWC data (Abeysekara et al. 2017b).

3. ANALYSIS

3.1. Background Estimation

The positions of the events are binned in equatorial coordinates using the HEALPix scheme (Gorski et al. 2005). For the analysis we set the pixel size to be $\sim 0.11^\circ$.

The background is estimated using the direct integration (DI) technique described in Atkins et al. (2003). The background is integrated over 24 hours and therefore only data were used when the detector performance was stable for 24 hours, since this is a requirement for the integration technique. This results in a lifetime for the analysis of 290 days.

As explained in Abeysekara et al. (2014), an analysis based on a background integration period of δt is sensitive to potential signal excesses of an RA size smaller than $\delta t \cdot 15^\circ \text{ hour}^{-1}$. Using a 24 hour integration period ensures that the analysis is sensitive to the Fermi Bubbles which extend to $\sim 50^\circ$ in RA.

Since the estimation of the background can be biased by strong known sources in the data, a *region of interest* (ROI) masking is used, as shown in Figure 1. The

ROI masking covers the galactic plane $[\pm 6^\circ]$, circular regions of 3° , 1.3° , 1° and 1° , respectively, for Geminga, the Crab Nebula, Mrk 421 and 501. Region A and B from the small-scale cosmic-ray anisotropy are also masked. Their shapes are obtained from the results in Abeysekara et al. (2014), by requiring that the significances in the cosmic-ray sky map are greater than 4σ . The ROI for the Northern *Fermi* Bubble was obtained from the *Fermi* Diffuse Model pass 7 version 6¹.

The shape of the Northern *Fermi* Bubble above 1 TeV is unknown. We perform a gamma-ray flux excess search within the boundaries of the Northern Bubble as detected by *Fermi* below TeV energies.

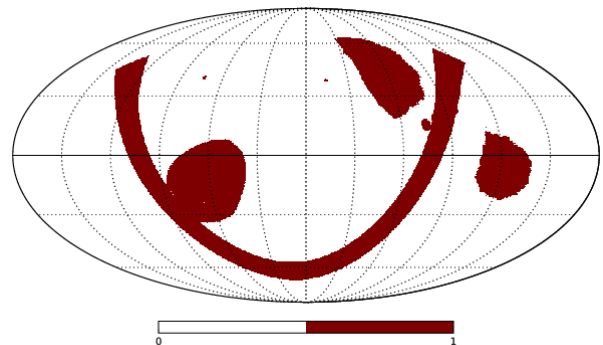


Figure 1. Sky map in equatorial coordinates showing the region of interest masking as used for the analysis as a counter for known sources contributing to the background.

3.2. Gamma-Ray Excess Calculation

The gamma-ray excess is calculated after the background estimation. However, gamma-hadron separation is not perfect. It is expected that the large-scale anisotropy from cosmic rays is present in the gamma-ray maps in the analysis bins where there is enough statistics to calculate the background with an accuracy of one part per mille (Abeysekara et al. 2013). As it will be seen in Section 4, the all-sky excess map in the analysis bin f_1 reveals the large-scale anisotropy as seen in the cosmic-ray map. The Northern *Fermi* Bubble is located at a deficit region, therefore this systematic effect needs to be removed. The subtraction of this cosmic-ray feature is done by using the data from cosmic-ray maps. The following is a description of our procedure for this removal.

For both gamma and cosmic-ray sky maps, the event excess is calculated by subtracting the estimated back-

¹ See <http://fermi.gsfc.nasa.gov/ssc/data/access/lat/BackgroundModel>.

ground from the data. The excess in the cosmic-ray (E_C) and the gamma-ray (E_G) maps are composed of cosmic rays (C) and gamma rays (G), but the composition is different in the gamma-ray maps due to the gamma-hadron cuts. This can be written as

$$\begin{aligned} E_C &= N_C - \langle N_C \rangle = C + G, \text{ and} \\ E_G &= N_G - \langle N_G \rangle = \varepsilon_C C + \varepsilon_G G, \end{aligned} \quad (1)$$

where N_C , N_G are the number of events in cosmic and gamma ray maps in each skymap pixel; $\langle N_C \rangle, \langle N_G \rangle$ are the estimated number of background events in cosmic and gamma ray maps in each skymap pixel; and ε_C and ε_G are the hadron and gamma passing rates after applying the gamma-hadron cuts. The hadron passing rate efficiency ε_C is obtained from the data assuming that most of the events are cosmic rays $\varepsilon_C \approx N_G/N_C$.

The gamma passing rate efficiency ε_G is obtained using simulations. The detector response is simulated in each of the seven analysis bins and for 5° declination bands between -37.5° and 77.5° . Each bin contains an energy histogram that is expected for the simulated signal. We compute the total number of events in the energy histograms and the ratio for the events with cuts $h_G(e)$ over the events with no cuts $h_C(e)$, where e is the energy. Therefore, the efficiency can be written as

$$\varepsilon_G = \frac{\int h_G(e) de}{\int h_C(e) de}. \quad (2)$$

The number of gamma rays obtained from the event excesses (Eq. 1) is

$$G = \frac{E_G - \varepsilon_C E_C}{\varepsilon_G - \varepsilon_C}. \quad (3)$$

The previous equation is used to calculate the number of gamma rays G in each pixel inside the Northern Bubble region as defined in Figure 1 and then summed to get a total excess. The equation describes how the cosmic-ray features are subtracted from the gamma-ray maps. As mentioned in Section 3.1, the shape of the Fermi Bubbles at high energies is unknown, though some authors suggest that the size of the bubbles increases with energy (Fujita et al. 2013; Yang et al. 2014; Mou et al. 2015). In this case, calculating the flux in the smaller region of the MeV-GeV excess is the more conservative approach.

The error calculation for G is obtained through

$$\begin{aligned} \left(\frac{\delta G}{|G|}\right)^2 &= \frac{\langle N_G \rangle + (E_C \varepsilon_C)^2 \left(2 \frac{\langle N_C \rangle}{N_C^2} + \frac{\langle N_G \rangle}{N_G^2}\right)}{(E_G - E_C \varepsilon_C)^2} \\ &+ \frac{\varepsilon_C^2 \left(\frac{\langle N_C \rangle}{N_C^2} + \frac{\langle N_G \rangle}{N_G^2}\right)}{(\varepsilon_G - \varepsilon_C)^2}. \end{aligned} \quad (4)$$

The efficiency ε_G is applied to the number of gamma rays G to obtain the number of excess events measured by the detector. The excess becomes

$$E = \varepsilon_G (G \pm \delta G). \quad (5)$$

3.3. Testing the Analysis Method

The analysis method is tested on simulated sky maps containing a dipole distribution as shown in Figure 2 assuming no sources are present. A rate map in the local

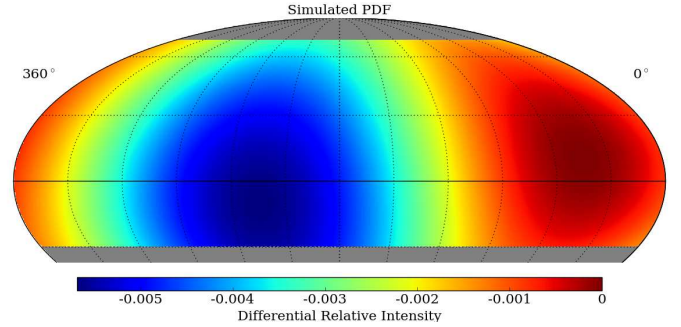


Figure 2. Dipole distribution used for the skymap simulation.

coordinates of HAWC containing a snapshot of 24 sec of data is generated. Since HAWC observations cover a local sky of zenith angles $0^\circ < \theta < 45^\circ$, the rate map is generated for this zenith angle range. Using the dipole distribution given in Figure 2, the total sky event rate from HAWC data, and information from the detector response, a rate in each pixel is obtained. After the 24 sec period the rate map is reset and the procedure is started again. In this way a simulated data set is generated that is of the same size as the real data set analyzed in this paper. An example of a resulting fake sky map f_1 is shown in Figure 3. The upper panel presents the resulting map after simply subtracting the estimated background from the data, the lower panel shows the excess map after applying the procedure described in Section 3.2.

Figure 4 shows the resulting simulated excesses in each f bin (red points). For comparison, the event excesses derived from simply subtracting the estimated DI background from the fake data (blue points). The effect of the large-scale anisotropy results in systematically lower excesses for the lowest two f bins if the method from Section 3.2 is not applied.

The method is also tested by adding a strong *Fermi* Bubble-like emission. The spectrum is assumed to be a power-law with spectral index $\gamma = 2.0$ and normalization of $5.03 \times 10^{-7} \text{ GeV}^{-1} \text{ cm}^{-2} \text{ s}^{-1} \text{ sr}^{-1}$, both values obtained by fitting the *Fermi* data points in the range of 1 GeV to 150 GeV. Figure 5 shows the ratio of the calculated excess to the expected excess ME . The cal-

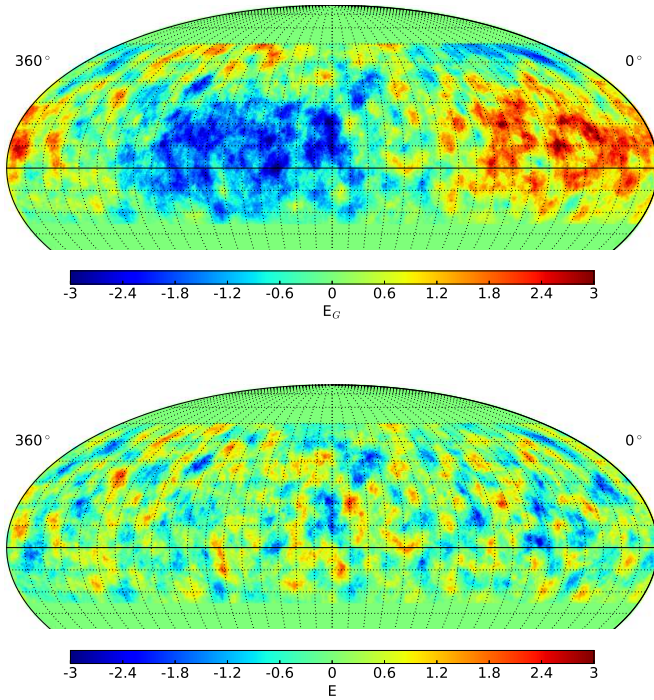


Figure 3. Simulated event excess in f_1 , smoothed with a 5° top-hat. *Top:* Event excess after subtracting the estimated background from the fake data. *Bottom:* Large-scale structure is removed after the method described in Section 3.2 is applied.

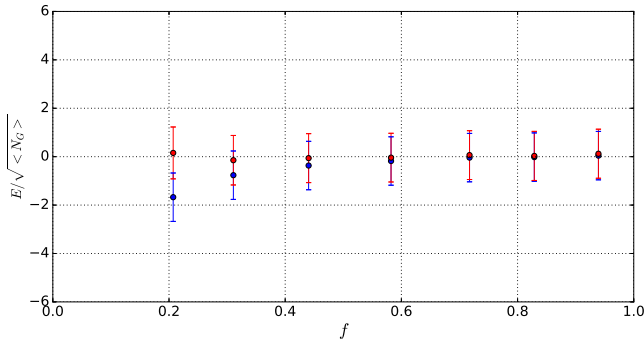


Figure 4. Simulated event excess inside the Northern Bubble region. The effect of the dipole is stronger at lower values of f . Blue: Estimated DI background subtracted from fake data; Red: Background subtraction considering the gamma and cosmic-ray efficiencies. See method described in Section 3.2.

culated excess is shown for before (blue) and after (red) the procedure. A ratio of one means that the calculated excess is the same as the expected excess.

4. RESULTS AND DISCUSSION

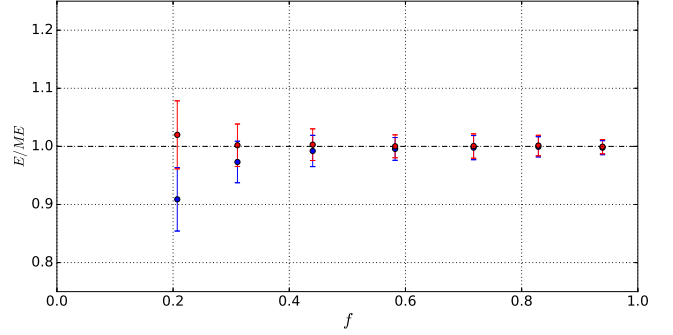


Figure 5. Simulated event excess inside the Northern Bubble region with a strong *Fermi* Bubble-like emission. The effect of the dipole is seen at lower values of f . Blue: Estimated DI background subtracted from fake data; Red: Background subtraction considering the gamma and cosmic-ray efficiencies. See method described in Section 3.2.

4.1. Gamma-Ray Excess Results

Figure 6 shows skymaps of the result of the first analysis bin, f_1 . The figure shows a cosmic-ray map, and gamma-ray maps before and after applying our procedure.

Figure 7 shows the results of the summed excess inside the bubble region after applying our procedure. No significant excess inside the bubble region is observed, therefore upper limits on the differential flux are calculated. The upper limits are also compared to the differential sensitivity of the HAWC observatory. The upper limits give the maximum flux intensity that is plausible given the observed counts in the HAWC data. The differential sensitivity quantifies the power of the detection procedure and is based on finding an α -level threshold (related to background fluctuations claimed as detections) and the probability β to detect a source².

4.1.1. Calculating the Upper Limits

The differential flux is calculated from the measured excess by comparing the signal observed in the data to an expected signal obtained for each of the fractional f analysis bins using simulations. Since the energy response histograms for each analysis bin overlap (see Figure 8), the excesses measured in the analysis bins are combined in a weighted sum.

The procedure is as follows: a differential flux is assumed in an energy bin of width $\Delta \log(E/1 \text{ TeV})$. The width of differential energy bins is defined such that the results are independent of spectral assumptions. Using the HAWC detector response, an expected signal for the

² The definitions of upper limit and sensitivity are the same as upper bound and upper limit in [Kashyap et al. \(2010\)](#).

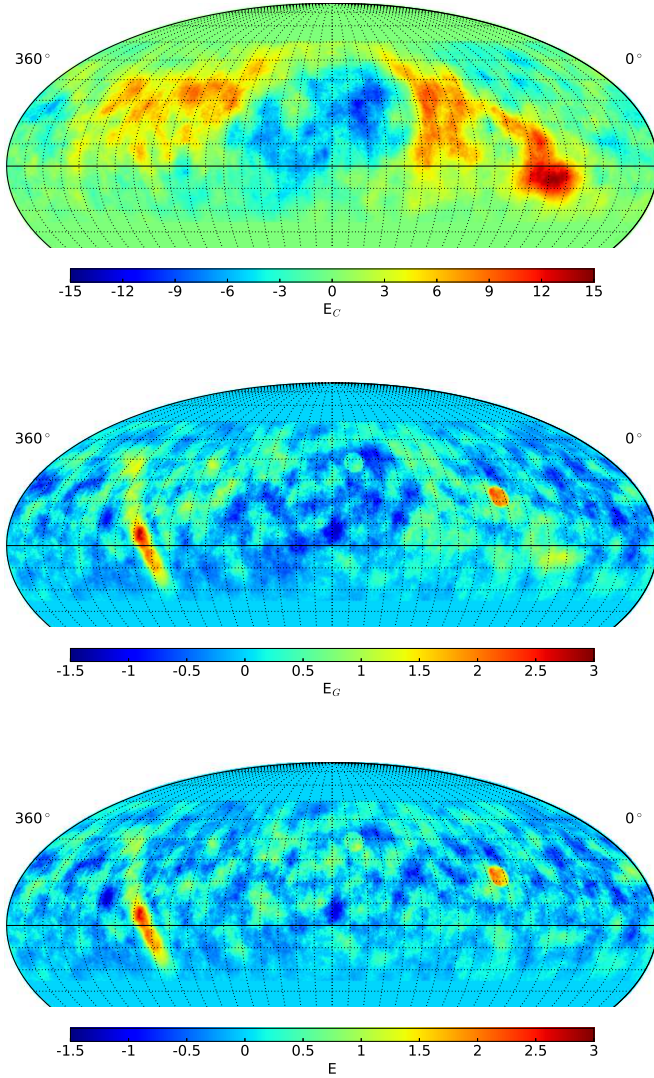


Figure 6. Event excesses in analysis bin f_1 , smoothed with a 5° tophat. *Top:* Event excess E_C after subtracting the estimated DI background from the cosmic-ray data. The large-scale CR anisotropy is visible. *Middle:* Event excess E_G after subtracting the estimated DI background from the gamma-ray data. A deficit caused by the large-scale anisotropy is visible. *Bottom:* Large-scale CR anisotropy structure is removed after the method described in Section 3.2 is applied.

Northern Bubble region is obtained for each fractional f bin. Taking into account the previous values, the weight in the energy bin k for the fractional bin f_i is calculated as

$$w_i^k = \frac{ME_i^k}{\langle N_G \rangle_i}, \quad (6)$$

where w_i^k is the weight in the energy bin k for the fractional f bin i ; ME_i^k is the expected signal in the energy bin k for the fractional f bin i , and $\langle N_G \rangle_i$ is the back-

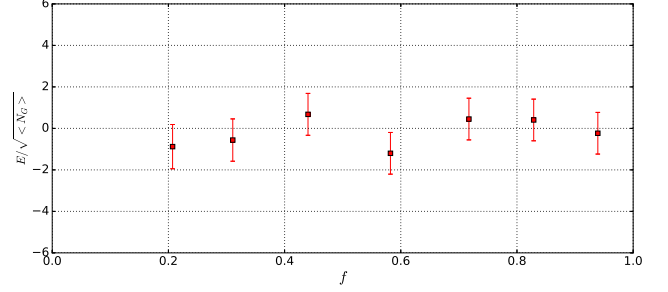


Figure 7. Event excess inside the Northern Fermi Bubble region after applying the procedure described in Section 3.2.

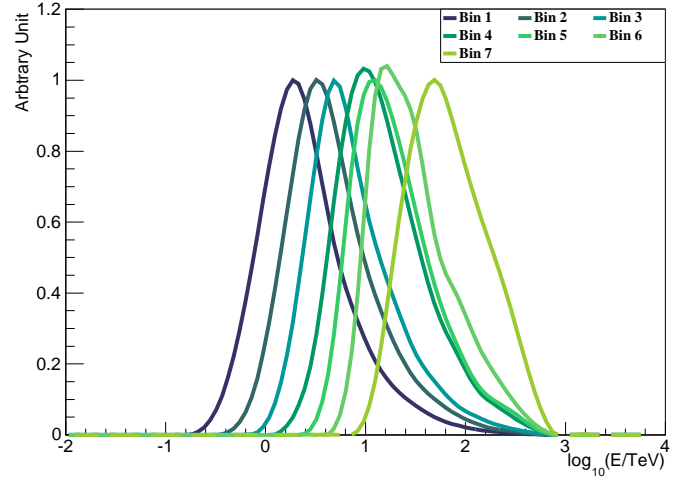


Figure 8. Energy distributions for the analysis bins assuming a 2.75 power-law spectrum.

ground estimated in fractional f bin i . This procedure results in a matrix that allows “projection” of the fractional f analysis bin space onto the energy space.

Using the weights, the ratio of the observed signal and the expected signal is calculated

$$R_k = \frac{\sum_{i=1}^f w_i^k E_i}{\sum_{i=0}^f w_i^k ME_i^k}, \quad (7)$$

and the uncertainty in the ratio as

$$\delta R_k = \frac{\sqrt{\sum_{i=1}^f (w_i^k \delta E_i)^2}}{\sum_{i=1}^f w_i^k ME_i^k}. \quad (8)$$

The ratio is used to obtain an estimation of the flux in the energy bin k

$$F_k = (R \pm \delta R)_k F(E_k). \quad (9)$$

The upper limit calculation is then performed in the energy bins. The prescription of [Helene \(1983\)](#) is used to calculate an upper limit on the differential flux derived from equation 9. A 95% confidence level is chosen.

4.1.2. Calculating the Sensitivity

The sensitivity is calculated based on [Kashyap et al. \(2010\)](#)³. The procedure consists of setting a small probability for false positives (Type I error) and setting a probability of detection when there is a source (related to Type II error). The probability for false positives is set to $\alpha = 0.05$ and the probability of detection is set to $\beta = 0.5$.

The calculation is performed by using the measured background and doing simulations for a fake *Fermi* Bubble of varying flux. For the simulation we assume a power-law with an index of -2.75 in the differential energy bin. For each analysis bin, the total background counts and the total expected number of events from the fake source are calculated inside the bubble region. Following the same procedure as in Section 4.1.1, the analysis bins are combined to get the total number of events for each energy bin. In each energy bin, a null hypothesis histogram and an alternative hypothesis histogram are created for the quantity

$$S_k = E_k / \sqrt{\langle N_G \rangle_k}, \quad (10)$$

where E_k is obtained by Poisson-fluctuating $\langle N_G \rangle_k$ for the null hypothesis, and then subtracting $\langle N_G \rangle_k$ from this value; or by Poisson-fluctuating $\langle N_G \rangle_k + ME_k$ for the alternative hypothesis, and then subtracting $\langle N_G \rangle_k$ from this value. The Poisson fluctuations are performed 10000 times to fill the histograms. The null hypothesis histogram is used to find the α -level detection threshold and the alternative hypothesis histogram is used to find the flux normalization that is required to obtain a probability of detection of 0.5.

4.2. Differential Flux of the *Fermi* Bubbles

The first energy bin is centered at 2.2 TeV, which is the median energy of fraction f_1 assuming a power law spectrum of index $\gamma = 2.75$ (see Figure 8). The energy bin width is set to $\Delta \log(E/1 \text{ TeV}) = 0.5$ which is comparable to the width of the energy histograms. The energy range covers up to the highest energy at which HAWC is sensitive (~ 100 TeV).

Table 2 shows the values of the upper limits and sensitivities for each energy bin. The upper limits obtained from data are consistent with the detection power of

HAWC. Figure 9 shows the upper limits together with the flux measurement of the *Fermi* Bubbles made by the *Fermi* Collaboration ([Ackermann et al. 2014](#)). Different leptonic and hadronic models are also present in Figure 9.

The two leptonic models are obtained from [Ackermann et al. \(2014\)](#). In these models, the emission is described by inverse Compton scattering. Two radiation fields are used: the IRF at 5 kpc above the Galactic Plane and photons from the CMB. The electron spectrum interacting with the radiation fields is modeled as a power-law with an exponential cutoff. The spectral index has a value of $2.17 \pm 0.5^{+0.33}_{-0.89}$ and the cutoff energy is $1.25 \pm 0.13^{+1.73}_{-0.68}$ TeV.

The two cyan hadronic models, also obtained from [Ackermann et al. \(2014\)](#), assume a power-law and a power-law with cutoff for the injection spectrum of the hadrons. These protons interact with the ISM producing neutral pions that decay into gamma rays. The spectrum was obtained using the library `cparamlib`⁴, which implements the cross sections from [Kamae et al. \(2006\)](#), for the production of gamma rays through hadronic interactions. The spectral index for the power-law is 2.2; the spectral index for the power-law with cutoff is $2.13 \pm 0.01^{+0.15}_{-0.52}$ with a cutoff energy of $14 \pm 7^{+6}_{-13}$ TeV. Using the fit results obtained in [Ackermann et al. \(2014\)](#), we extrapolate the results for the hadronic models above 100 TeV. The upper limits derived from HAWC data exclude the hadronic injection without a cutoff, that best fits the GeV gamma-ray data, above 3.9 TeV.

The hadronic model represented by the red line is obtained from [Lunardini et al. \(2015\)](#). This model is the counterpart of a neutrino flux model that best fits the IceCube data. The IceCube data corresponds to five events that are spatially correlated with the *Fermi* Bubbles. The differential flux model was obtained by taking into account the flux from both bubbles. Above 10 TeV, the HAWC upper limits exclude the parent proton spectrum predicted from IceCube data.

Table 3 gives a summary of the different models.

Early reports such as [Crocker & Aharonian \(2011\)](#); [Fujita et al. \(2013\)](#), presented the possibility of observing TeV gamma rays. The intensity was predicted to be $\leq E^2 F(\text{TeV}) \sim 10^{-6} \text{ GeVcm}^{-2}\text{s}^{-1}\text{sr}^{-1}$. The result presented here sets a stricter upper limit.

The result is not constraining the main contribution to the spectrum of the *Fermi* Bubbles. Nevertheless our result may imply, for a hadronic model, that there is a cutoff in the proton spectrum. [Ackermann et al. \(2014\)](#)

³ Named upper limit in the reference instead of sensitivity

⁴ <https://github.com/niklask/cparamlib>

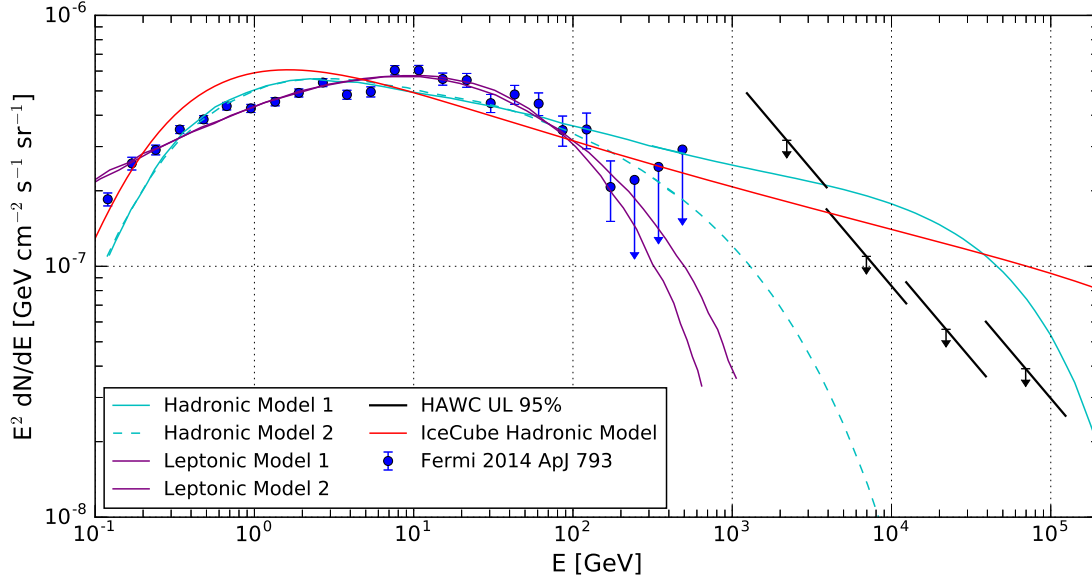


Figure 9. HAWC upper limits together with the *Fermi* data and gamma-ray production models from Ackermann et al. (2014) and Lunardini et al. (2015). See table 3 for spectral assumptions of these models.

Table 2. Characteristics of the non-detection: upper limits on the differential flux

Energy Range [TeV]	Upper Limits [GeVcm ⁻² s ⁻¹ sr ⁻¹]	Sensitivity [GeVcm ⁻² s ⁻¹ sr ⁻¹]
1.2 - 3.9	3.0×10^{-7}	3.3×10^{-7}
3.9 - 12.4	1.0×10^{-7}	1.1×10^{-7}
12.4 - 39.1	0.5×10^{-7}	0.5×10^{-7}
39.1 - 123.7	0.4×10^{-7}	0.3×10^{-7}

showed that GeV gamma-ray spectrum cuts off around 100 GeV. The cutoff for the parent proton spectrum in this case could be around 1 TeV (Cheng et al. 2015).

As mentioned in Section 3.2, Fujita et al. (2013); Yang et al. (2014); Mou et al. (2015) propose that the size of the bubbles increases with energy. While defining the search region to be the same as the excess detected at GeV energies is a more conservative approach, it may be interesting to increase the size of the latter in a follow-up analysis.

Increasing the sensitivity at energies < 1 TeV is another objective for future analysis. Compared to recent (Abeysekara et al. 2017b,a) or future (HAWC Collaboration 2017, in preparation) publications of the analysis of HAWC data, this analysis uses only the seven highest event-size bins. At energies $\lesssim 1$ TeV, the large-scale

anisotropy signal (or any significant, spatially-extended feature) causes signal contamination in the estimation of the background because the structure takes up a large portion of the field-of-view of HAWC, significantly altering the all-sky rate. An iterative procedure for the DI method will be followed as explained in Ahlers et al. (2016) and has been shown to remove this artifact.

5. CONCLUSIONS

A search of high-energy gamma rays in the Northern *Fermi* Bubble region has been presented by using 290 days of data from the HAWC observatory. No significant excess is found above 1.2 TeV in the search area and the 95% C.L. flux upper limits are calculated and compared to the differential sensitivity with $\alpha = 0.05$ and $\beta = 0.5$. The upper limits are between 3×10^{-7} GeV cm⁻² s⁻¹ sr⁻¹ and 4×10^{-8} GeV cm⁻² s⁻¹ sr⁻¹. The upper limits, for gamma-ray energies between 3.9 TeV and 120 TeV, disfavor the emission of hadronic models that try to explain the GeV gamma-ray emission detected by the *Fermi* LAT. This makes a continuation of the proton injection above 100 TeV highly unlikely (solid cyan line in Figure 9). The HAWC upper limits also disfavor a hadronic injection spectrum derived from IceCube measurements. The present result does not allow unequivocal conclusions about the hadronic or leptonic origin of the *Fermi* bubbles though. A future analysis of HAWC data will include a better sensitivity, especially at lower ener-

Table 3. Differential flux models for the *Fermi* Bubbles

Model	Description
Hadronic Model 1	$N_p \propto p^{-2.2}$
Hadronic Model 2	$N_p \propto p^{-2.1} \exp(-pc/14 \text{ TeV})$
Leptonic Model 1	$N_e \propto p^{-2.17} \exp(-pc/1.25 \text{ TeV})$ and IRF at 5kpc
Leptonic Model 2	$N_e \propto p^{-2.17} \exp(-pc/1.25 \text{ TeV})$ and CMB
IceCube Hadronic Model	$N_p \propto p^{-2.25} \exp(-pc/30 \text{ PeV})$

gies and possibly larger search regions according to the predictions of some theoretical models.

We acknowledge the support from: the US National Science Foundation (NSF); the US Department of Energy Office of High-Energy Physics; the Laboratory Directed Research and Development (LDRD) program of Los Alamos National Laboratory; Consejo Nacional de Ciencia y Tecnologia (CONACyT), Mexico (grants 271051, 232656, 260378, 179588, 239762, 254964, 271737, 258865, 243290, 132197), Laboratorio Nacional HAWC de rayos gamma; L'OREAL Fellowship for Women in Science 2014; Red HAWC, Mx-

ico; DGAPA-UNAM (grants RG100414, IN111315, IN111716-3, IA102715, 109916, IA102917); VIEP-BUAP; PIFI 2012, 2013, PROFOCIE 2014, 2015; the University of Wisconsin Alumni Research Foundation; the Institute of Geophysics, Planetary Physics, and Signatures at Los Alamos National Laboratory; Polish Science Centre grant DEC-2014/13/B/ST9/945; Coordinacin de la Investigacin Cientfica de la Universidad Michoacana. Thanks to Luciano Daz and Eduardo Murieta for technical support. We thank Cecilia Lunardini for providing us with the gamma-ray flux model from IceCube data.

REFERENCES

- Abeyssekara, A., et al. 2013, *Astroparticle Physics*, 5052, 26
— 2014, *ApJ*, 796, 108
- Abeyssekara, A. U., Albert, A., Alfaro, R., et al. 2017a, ArXiv e-prints
— 2017b, ArXiv e-prints
- Ackermann, M., Albert, A., et al. 2014, *ApJ*, 793, 64
- Ahlers, M., BenZvi, S. Y., Desiati, P., et al. 2016, *The Astrophysical Journal*, 823, 10
- Atkins, R., Benbow, W., Berley, D., et al. 2003, *ApJ*, 595, 803
- Cheng, K. S., Chernyshov, D. O., Dogiel, V. A., & Ko, C. M. 2015, *The Astrophysical Journal*, 804
- Cheng, K.-S., Chernyshov, D. O., Dogiel, V. A., Ko, C. M., & Ip, W. 2011, *The Astrophysical Journal*, 731, L17
- Crocker, R. M., & Aharonian, F. 2011, *Physical Review Letters*, 106, 101102
- Dobler, G., Finkbeiner, D. P., Cholis, I., Slatyer, T. R., & Weiner, N. 2010, *ApJ*, 717, 825
- Fujita, Y., Ohira, Y., & Yamazaki, R. 2013, *The Astrophysical Journal Letters*, 775, 20
— 2014, *The Astrophysical Journal*, 789
- Gorski, K., Hivon, E., Banday, A., et al. 2005, *ApJ*, 622, 759
- Guo, F., & Mathews, W. G. 2012, *The Astrophysical Journal*, 756, 181
- Guo, F., Mathews, W. G., Dobler, G., & Oh, S. P. 2012, *The Astrophysical Journal*, 756, 182
- HAWC Collaboration. 2017, in preparation
- Helene, O. 1983, *Nucl. Instrum. Methods Phys. Res.*, 212, 319
- Kamae, T., Karlsson, N., Mizuno, T., et al. 2006, *ApJ*, 647, 692
- Kashyap, V. L., van Dyk, D. A., Connors, A., Freeman, P. E., Siemiginowska, A., Xu, J., & Zezas, A. 2010, *The Astrophysical Journal*, 719, 900
- Lunardini, C., Razzaque, S., & Yang, L. 2015, *Phys. Rev. D*, 92, 021301
- Mou, G., Yuan, F., Gan, Z., & Sun, M. 2015, *The Astrophysical Journal*, 811, 37
- Su, M., Slatyer, T. R., & Finkbeiner, D. P. 2010, *ApJ*, 724, 1044
- Yang, R.-Z., Aharonian, F., & Crocker, R. 2014, *A&A*, 567, 8